AIAA JOURNAL
Vol. 56, No. 5, May 2018

Effect of Nozzle–Plate Distance on Acoustic Phenomena from Supersonic Impinging Jet

Masahito Akamine* and Koji Okamoto†
University of Tokyo, Chiba 277-8561, Japan
Kent L. Gee‡ and Tracianne B. Neilsen§
Brigham Young University, Provo, Utah 84602
Susumu Teramoto¶ and Takeo Okunuki**
University of Tokyo, Tokyo 113-8656, Japan
and
Seiji Tsutsumi††
Japan Aerospace Exploration Agency, Kanagawa 252-5210, Japan

DOI: 10.2514/1.J056504

For an adequate understanding of the broadband acoustic phenomena generated by a rocket exhaust jet impinging on a flame deflector, this study experimentally clarifies the factors that cause the difference in the broadband acoustic field of a supersonic ideally expanded jet impinging on an inclined flat plate for various nozzle–plate distances. According to previous studies, there are two possible factors: the Mach waves, which are radiated from the free-jet region and reflected by the plate, and the acoustic waves generated in the impingement region. To distinguish the effects of these factors, this study compares the following three results: the overall sound pressure level distribution, images extracted from the schlieren visualization movies using acoustic-triggered conditional sampling, and tracing lines of the acoustic intensity vectors of the Mach waves. The results reveal that the nozzle–plate distance affects the fraction of the Mach waves that are generated in the free-jet region and reflected by the plate, resulting in a higher overall sound pressure level in the upstream direction for larger nozzle–plate distances. It is concluded that the location of the plate relative to the source region of the Mach waves significantly affects the acoustic phenomena, owing to the variation in the nozzle–plate distances.

I. Introduction

FOR the development of launch vehicles and launch pads, the level of acoustic loading at liftoff must be predicted accurately and suppressed to a level that is acceptable. To achieve this, it is essential to identify the sources of acoustic loading. One of the sources is the acoustic phenomenon generated by the supersonic exhaust jet of rocket engines. As the exhaust jet impinges on a flame deflector on the ground, the acoustic waves generated due to the jet impingement will also cause acoustic loading in addition to the acoustic waves from the freestream of the exhaust jet. Therefore, an adequate understanding of the acoustic phenomena due to a supersonic impinging jet is required.

Supersonic impinging jets can generate both discrete and broadband noise. The discrete tones have been investigated in several studies, as reviewed by Henderson [1]. A typical flow discussed by Henderson [1] and references in this paper was a supersonic jet impinging on a large flat plate perpendicular to the jet for various nozzle pressure ratios and nozzle–plate distances. The flowfield of the supersonic impinging jet generally consists of the free-jet, jet-impingement, and wall-jet regions. An acoustic wave is generated from sources around the impingement region, and it propagates upstream and generates a large coherent structure of the free-jet region. This large coherent structure generates the acoustic wave around the impingement region again, and thus the feedback loop is formed. The flow structures around the impingement region are complicated and include the periodic oscillations of the shock structures and recirculation flow. Therefore, recent works have discussed the relation between the discrete tone and periodic oscillations [2–6] and the characteristics of the large coherent structures of the free-jet region [7–9].

In the case of a jet impinging on an inclined flat plate, the broadband noise is dominant, and the noise generation mechanism is complicated. These have been initially studied in the work of Nonomura et al. [10], which included the numerical simulation of a Mach 2 ideally expanded jet impinging on a 45 deg inclined flat plate with a nozzle–plate distance of 5 nozzle-exit diameters. Nonomura et al. [10] suggested that the acoustic field associated with this jet consists of three acoustic phenomena, as illustrated in Fig. 1a: the Mach waves from the free-jet region (i), the acoustic waves generated in the impingement region (ii), and the Mach waves from the wall-jet region (iii). The Mach waves are acoustic waves specific to the supersonic shear layer, which are generated owing to the supersonic convection of the large coherent structures, as explained by Tam [11]. The acoustic waves (ii) are radiated from the impingement region and propagate in a direction almost perpendicular to the inclined flat plate. This suggestion of Nonomura et al. [10] was consistent with the observations of subsequent studies involving similar impinging jets, such as the numerical simulations of Tsutsumi et al. [12,13], Brehm et al. [14], and Nonomura et al. [15] and the experimental works of Worden et al. [16,17] and Akamine et al. [18,19]. For example, Akamine et al. [19] experimentally observed the complicated acoustic waves around the impinging jet, which corresponded to the

Presented as Paper 2016-2930 at the 22nd AIAA/CEAS Aeroacoustics Conference, Lyon, France, 30 May–1 June 2016; received 6 July 2017; revision received 2 December 2017; accepted for publication 2 February 2018; published online 30 March 2018.

*Ph.D. Student, Department of Advanced Energy, Graduate School of Frontier Sciences. Student Member AIAA.
†Associate Professor, Department of Advanced Energy, Graduate School of Frontier Sciences. Member AIAA.
‡Professor, Department of Physics and Astronomy, N283 ESC. Member AIAA.
§Part-time Assistant Professor, Department of Physics and Astronomy, N283 ESC. Member AIAA.
¶Professor, Department of Aeronautics and Astronautics, Graduate School of Engineering. Senior Member AIAA.
**Engineer, Department of Aeronautics and Astronautics, Graduate School of Engineering.
††Associate Senior Researcher, Aerospace Research and Development Directorate, Research Unit III. Member AIAA.

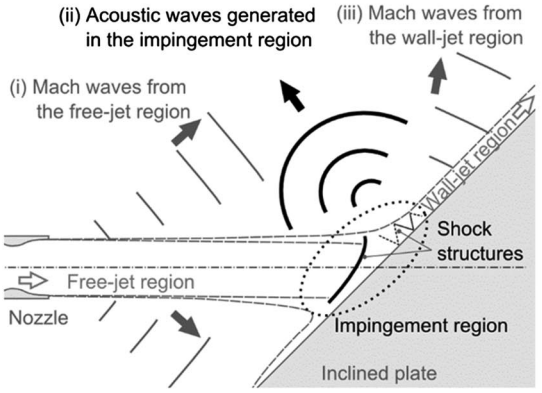

a) Schematic

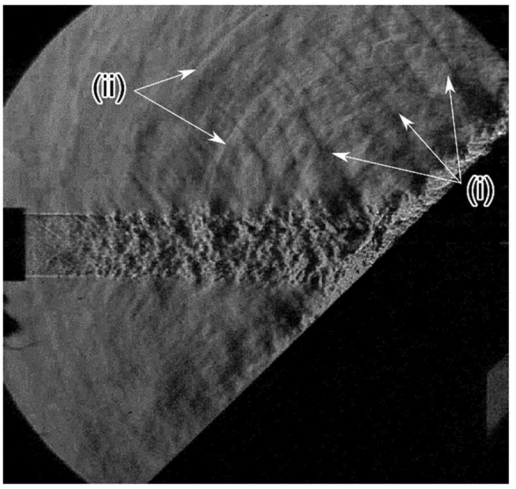

b) Schlieren image [19]: Mach waves from the free-jet region (point i), and acoustic waves generated in the impingement region (point ii)

Fig. 1 Acoustic phenomena from supersonic impinging jet.

Mach waves (i) from the free-jet region and acoustic waves (ii) from the impingement region, as shown in the schlieren image in Fig. 1b; the Mach waves (iii) are not observed in the visualization region of Fig. 1b because they are generated in the wall-jet region further downstream, as observed in [18].

The impingement conditions can have a large impact on the characteristics of the broadband acoustic field associated with the supersonic impinging jet. Although a complicated interaction between the flow structures and the impingement region needs more investigation, the nozzle–plate distance has a pronounced effect on the acoustic phenomena. Understanding of the effects of the nozzle–plate distance is important not only for elucidating the noise generation mechanisms of an ideally expanded jet impinging on an inclined flat plate but also for predicting the acoustic noise field around the ascending launch vehicle. Comparisons of the characteristics of the acoustic fields of various nozzle–plate distances have been presented by Nonomura et al. [10] (5 and 10 nozzle-exit diameters), Worden et al. [16,17] (ranging from 2 to 12 nozzle-exit diameters), and Akamine et al. [19] (5 and 15 nozzle-exit diameters). Akamine et al. [19] found an interesting feature; the overall sound pressure level (OASPL) was higher in a part of the upstream region (in the direction approximately 75 deg from the inclined flat plate) in the case of the greater nozzle–plate distance. Two factors are supposed to be responsible for this increase in the OASPL. The acoustic waves (ii) may be one of these factors because it propagates in a similar direction. The Mach waves (i) from the free-jet region may also affect the upstream region owing to the reflection from the inclined flat plate, as suggested in the numerical simulation of the acoustic field at the launch pad conducted by Tsutsumi et al. [20]. However, the dominant factor is still unclear because the acoustic field is extremely complicated, and thus, the effects of these factors cannot be distinguished.

As explained previously, there are two factors that can contribute to the change in the broadband acoustic field on the upstream side (in the direction approximately 75 deg from the inclined flat plate) of the supersonic impinging jet due to the variation in the nozzle–plate distance: the acoustic waves generated in the impingement region and Mach waves that were generated in the free-jet region and reflected by the inclined flat plate. The objective of this study is to investigate how these factors affect the acoustic field. In addition to the sound pressure level (SPL) measurement, schlieren visualization movies with high spatial resolution are made to observe the complicated phenomena around the source region. An acoustic-triggered conditional sampling technique [19] is applied to these movies to extract phenomena that correlate to the targeted intermittent acoustic wave. Furthermore, a ray tracing of acoustic intensity vectors [21] is introduced to estimate the propagation region of the Mach waves (i) from the free-jet region. The result of this ray tracing aids in determining whether the waves extracted from the movies are the Mach waves (i) or the acoustic waves (ii) generated in the impingement region. Based on this observation, the effect of the nozzle–plate distance on the acoustic field is finally discussed.

II. Methods

A. Jet Facility

The experiment was performed at the Hypersonic and High-Enthalpy Wind Tunnel at the Kashiwa Campus of the University of Tokyo. Table 1 and Fig. 2 show the experimental condition and nomenclature. A Mach 1.8 ideally expanded jet was generated using an axisymmetric convergent–divergent nozzle (exit diameter $D = 20$ mm). This jet impinged on a 45 deg inclined flat plate. The nozzle–plate distance (o–o' in Fig. 2) was varied between $5D$ and $20D$. The detailed description of the jet facility, nozzle, and inclined flat plate can be found in [18]. Note that the inclined flat plate was sufficiently large (the end of the plate located at approximately $30D$ from the impingement region on the downstream side and $10D$ on the other three sides), and the influence of the end of the plate was negligible in the present discussion.

B. Sound Pressure Level Measurement

To observe the acoustic field, the SPL was measured using a single 1/4 in. free-field microphone (Type 4939, Brüel & Kjær) with a two-axis positioning system. The location of the microphone was represented by $(x/D, z/D)$ or (r, θ) shown in Fig. 2. Figure 3 shows the measurement points in the case of a nozzle–plate distance of $5D$. In the cases with various nozzle–plate distances, the location of the measurement points was fixed relative to the inclined flat plate. The signal was acquired using the National Instruments data acquisition device PCI-6133 and LabVIEW (sampling frequency = 400 kHz; signal length = 1 s). As described in [18], the narrow-band SPL (or power spectral density) was obtained using the fast Fourier transform and corrected with a

Table 1 Experimental condition

Parameter	Value
Jet Mach number M_j	1.8
Nozzle exit diameter D, mm	20
Stagnation pressure, MPa	0.575 ± 0.01
Stagnation temperature, K	291–305
Reynolds number Re_D	1.5×10^6
Nozzle–plate distance, D	5,10,15,20
Plate angle, deg	45

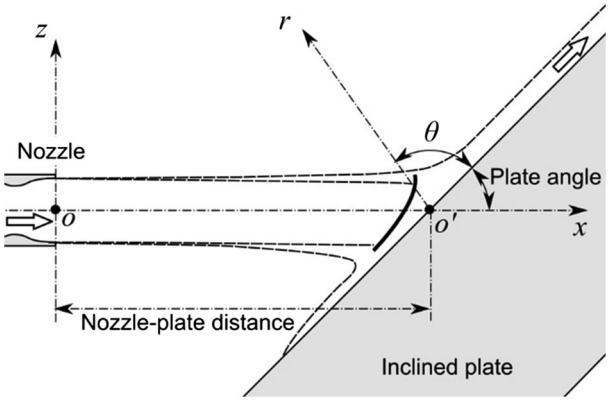

Fig. 2 Coordinate system and nomenclature.

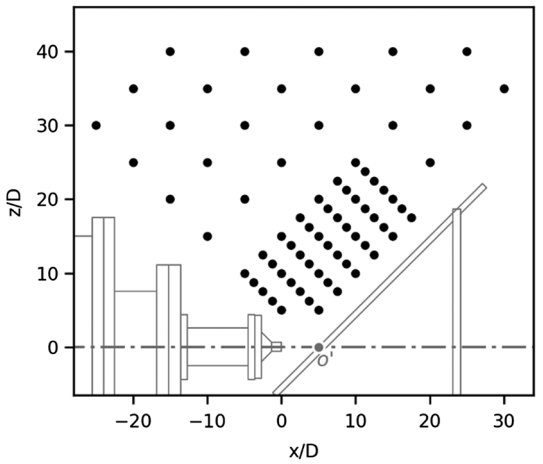

Fig. 3 SPL measurement points (nozzle–plate distance = 5*D*).

microphone free-field response curve of the incidence angle of 0 deg because the angle between the r axis (in Fig. 2) and the direction in which the microphone was pointed was less than 30 deg. The OASPL was then calculated using the SPLs of 1–40 kHz.

C. Conditional Sampling of Schlieren Visualization Movies

Schlieren visualization movies were used to observe the region around the free-jet and impingement regions. A conventional Z-type optical system consisting of a mercury lamp, a pair of concave mirrors (diameter = 200 mm; focal length = 2 m), a knife edge perpendicular to the jet axis, and a high-speed camera (Photron FASTCAM SA-Z; exposure time = 0.37 μs; frame rate = 100,000 frames per second; movie length = 1 s; resolution = 512×328 pixels) was used. For a nozzle–plate distance of 5*D*, the target region was covered with two movies recorded separately. The typical frames of these two movies are shown in Fig. 4a (movies 1 and 2). For a nozzle–plate distance of 15*D*, three movies were recorded separately, as shown in Fig. 4b (movies 3–5).

Figure 4 shows the density fluctuations due to the jet flow and acoustic waves. However, by observing only these raw movies, it was difficult to discuss the characteristics of the acoustic phenomena such as the location of the source region and correlations between the visualized phenomena. This motivated us to apply an extraction technique to these raw movies. In this study, the acoustic-triggered conditional sampling technique using the wavelet transform proposed by Akamine et al. [19] was employed. This technique is an extension of the conditional sampling such as Moore [22], Camussi and Guj [23], and Guj et al. [24] and differs from the other methods that involve the use of the wavelet transform, such as the wavelet filtering by Cavalieri et al. [25] and Kœnig et al. [26] and the method for detecting the periods of noise generation by Hileman et al. [27] and Kastner et al. [28].

In this technique, the acoustic signal was first recorded using a microphone simultaneously with the schlieren visualization movie. Then, intermittent acoustic waves at a target frequency (i.e., triggers) were detected from the acoustic signal. Finally, phenomena correlating to the triggers were extracted from the raw schlieren visualization movies. Figure 5 illustrates this technique, which consists of four steps: 1) trigger detection (from Fig. 5a to Fig. 5b), 2) phase adjustment (from Fig. 5b to Fig. 5c), 3) frame sampling (from Fig. 5c to Fig. 5d), and 4) averaging (from Fig. 5d to Fig. 5e).

In step 1, the time of the triggers at the target frequency was determined from the acoustic signal using the continuous wavelet transform. The triggers were defined as the local maxima in the map of the time variation of amplitude at each frequency, $|W|/\sqrt{s/\delta t}$, where $|W|$ was the absolute value of the wavelet coefficient of the sound pressure signal, and $|W|$ was divided by $\sqrt{s/\delta t}$ because the values of $|W|$ for unit-amplitude sine waves at different frequencies were almost proportional to $\sqrt{s/\delta t}$ (s was a scale factor, and δt was the time spacing of the signal). According to Torrence and Compo [29], the wavelet coefficient of the sound pressure signal p_n at time t_n ($t_n = n\delta t$, where $n = 0, \ldots, N-1$) and frequency f can be obtained as follows:

$$W(t_n, f) = \sum_{n'=0}^{N-1} p_{n'} \sqrt{\frac{\delta t}{s}} \psi^* \left(\frac{(n'-n)\delta t}{s} \right) \tag{1}$$

where ψ^* was the complex conjugate of a wavelet function ψ [in this study, the Morlet wavelet $\psi(t) = \pi^{-1/4} e^{i\omega_0 t} e^{-t^2/2}$ with $\omega_0 = 6$ was used], and the scale factor $s = (\omega_0 + \sqrt{2+\omega_0^2})/4\pi f$ for the Morlet wavelet. The local maximum was defined as a point that was the maximum in the 0.125 ms × 10 kHz window centered at the point. No threshold was set in this study, and it was confirmed that the influence of the threshold on the results was negligible. Figure 5a is a typical sound pressure signal p_n (normalized by the rms σ_p of p_n), and Fig. 5b is the map of $|W|/\sqrt{s/\delta t}$ of p_n. In Fig. 5b, the local maxima are represented by the cross marks. When the target frequency f_{target} is set at the frequency on the black dashed line, for example, three triggers indicated by the filled circles can be detected.

Next, in step 2, the times of the triggers were adjusted to match the phase of the triggers. This phase adjustment is needed to allow for

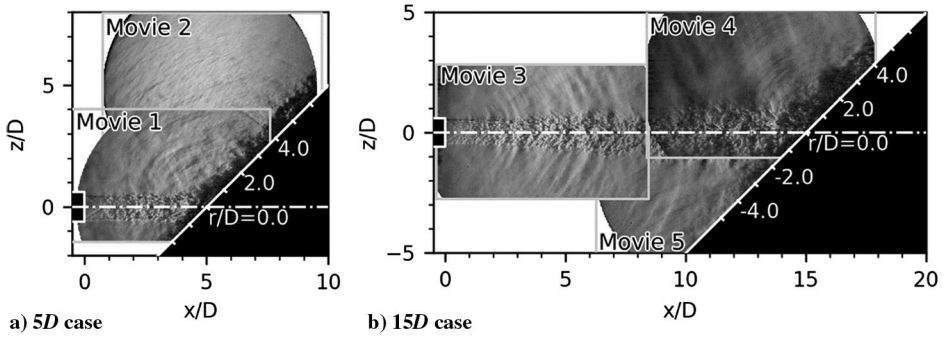

a) 5*D* case **b) 15*D* case**

Fig. 4 Raw schlieren images (movies 1–5 were recorded separately).

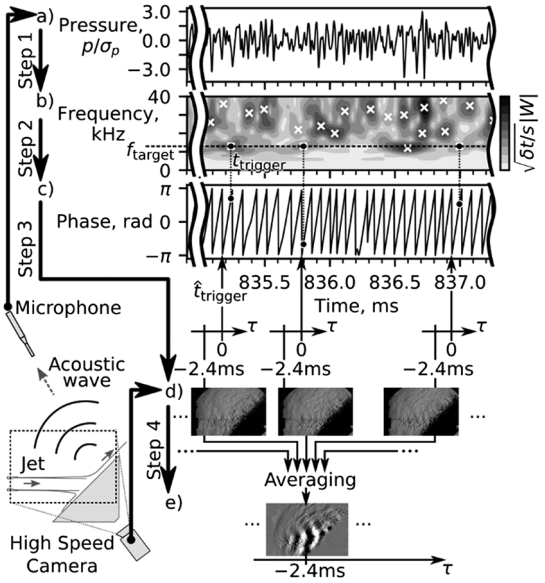

Fig. 5 Conditional sampling analysis proposed in [19].

coherence because the phase values at the local maxima of $|W|$ are not necessarily the same. Note that the phase value of the wavelet coefficient was $\phi(t_n, f) = \tan^{-1}\{\mathrm{Im}W(t_n, f)/\mathrm{Re}W(t_n, f)\}$ The time of a trigger detected in step 1, t_{trigger}, was adjusted to $\hat{t}_{\mathrm{trigger}}$ as follows:

$$\hat{t}_{\mathrm{trigger}} = t_{\mathrm{trigger}} - \frac{\phi_{\mathrm{trigger}} - \phi_{\mathrm{ref}}}{2\pi f_{\mathrm{target}}} \tag{2}$$

where $\phi_{\mathrm{trigger}} = \phi(t_{\mathrm{trigger}}, f_{\mathrm{target}})$, and ϕ_{ref} was the arbitrary reference phase value, which was set at $-\pi$ in this study. Figure 5c plots the phase values of the wavelet coefficients at the target frequency f_{target}. The phase values at the triggers detected in step 1 are plotted as the filled circles, and the adjusted times of triggers were indicated as the arrows.

Then, in step 3, frames at an offset time τ before the times of the triggers were sampled from the schlieren visualization movie. In Fig. 5d, for example, the sampled frames at $\tau = -2.40$ ms are shown. Finally, in step 4, the sampled frames were averaged, as shown in Fig. 5e. The averaged image shows the phenomena that correlate to the triggers and are captured in the schlieren visualization movie at 2.40 ms before every trigger. Moreover, the phenomena that were uncorrelated with the triggers are expected to be canceled by averaging. By varying the offset time τ, the correlated phenomena can be observed as a movie. Note that a time-averaged schlieren image was subtracted from the conditional average to observe fluctuations.

The extracted results depend on the location of the microphone and target frequency. The location of the microphone was $r/D = 40$ and $\theta = 75$ deg, at which a high OASPL was observed for both

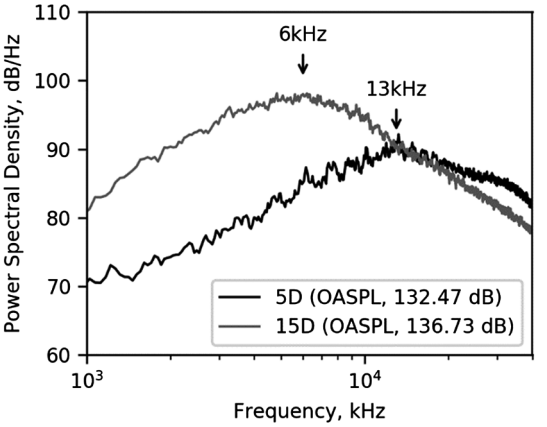

Fig. 7 SPL spectra at $r/D = 40$ and $\theta = 75$ deg.

the shorter and longer nozzle–plate distances ($5D$ and $15D$, respectively), as mentioned in [19] and shown in Fig. 6. The target frequency was set at 13 kHz (Strouhal number $St = 0.54$) in both the $5D$ and $15D$ cases. This target frequency corresponded to the peak frequency of the sound pressure level spectrum at $r/D = 40$ and $\theta = 75$ deg in the $5D$ case, as shown in Fig. 7. The target frequency was needed to be the same between the two cases because, if the target frequency differed depending on the cases, it may be hard to compare the extracted results owing to the wavelength difference. The peak frequency in the $15D$ case (approximately 6 kHz; $St = 0.25$) was not suitable for the comparison because the extraction cannot be performed in the $5D$ case by setting the target frequency at 6 kHz owing to shortage of the triggers. Note that it was confirmed that the target frequency did not change the extracted fluctuations significantly in the $15D$ case, except for the wavelength and gray values. Then, 300 triggers at 13 ± 1 kHz were used for the averaging. The microphone and data acquisition system used were the same as that in Sec. II.B. Although the movies were recorded asynchronously, the fixed microphone location and target frequency allow imaging of wave propagation across frame boundaries [19].

D. Ray Tracing of Acoustic Intensity Vectors

As described in Sec. I, the broadband acoustic field of the supersonic impinging jet is considered to consist of three acoustic phenomena: the Mach waves from the free-jet and wall-jet regions and the acoustic waves generated in the impingement region. Although this is a more complicated case, the free-jet intensity vectors give an approximation to the expected propagation region of the Mach waves in the impinging-jet case. Two assumptions were introduced; the acoustic intensity vectors obtained in the free-jet experiments were the same as those in the impinging jet experiments, except for the length of the source region, and the Mach waves were reflected specularly by the inclined flat plate. The second assumption was reasonable, in particular, in the lower side of the jet in the $15D$

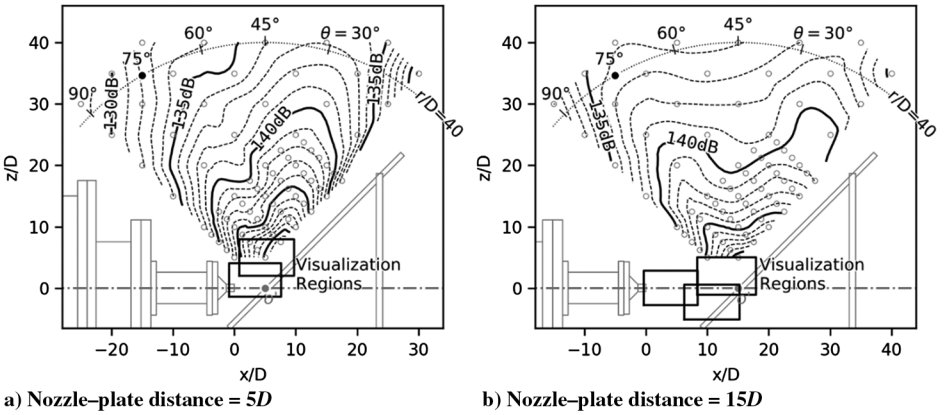

a) Nozzle–plate distance = $5D$ **b) Nozzle–plate distance = $15D$**

Fig. 6 OASPL distributions [19] (filled circle, $r/D = 40$ and $\theta = 75$ deg, where the microphone is located to detect the triggers).

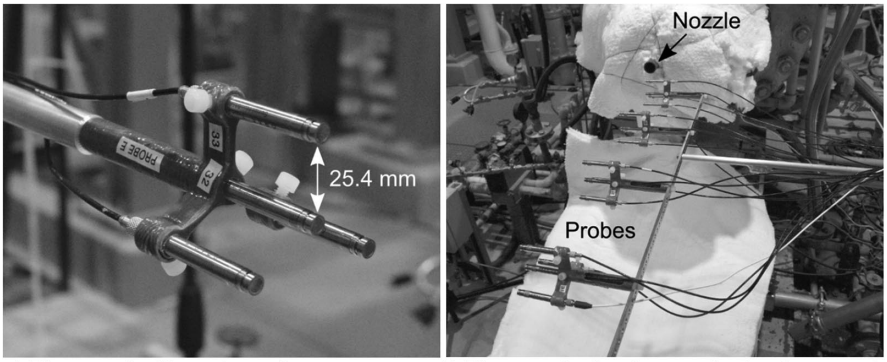

a) Photograph of intensity probe **b) Photograph of probes attached to the two-axis positioning system**

Fig. 8 Two-dimensional intensity probe.

case because the aluminum impingement plate was flat and smooth and because the flow was not observed on the plate surface beneath the jet in the raw schlieren image in Fig. 4b. Based on these assumptions, the propagation region of the Mach waves from the free-jet region can be estimated by using the ray-tracing technique in the impinging jet case.

The active acoustic intensity vector indicates both the intensity level and propagation direction at the location of the probe. At high frequencies, the vector can be obtained using the phase and amplitude gradient estimator method, which was proposed by Thomas et al. [30]. In this method, the active acoustic intensity vector $\boldsymbol{I}$ at a frequency f was formulated with the following equation presented by Mann et al. [31]:

$$\boldsymbol{I} = \frac{1}{\omega\rho_0} P^2 \nabla\phi \tag{3}$$

where $\omega = 2\pi f$, and ρ_0 was the density of the surrounding atmosphere. P was the effective value of pressure magnitude at frequency f, and $\nabla\phi$ was the phase gradient of the complex pressure at frequency f. The significant feature of this method was the phase unwrapping performed for calculating $\nabla\phi$, which enabled us to obtain the vectors at high frequencies. This method has been previously applied for measuring the vectors of a solid rocket motor [32] and laboratory-scale jet [21]. Furthermore, Gee et al. [32] estimated the location of the source region by backtracing these vectors.

This study made use of the acoustic intensity vectors obtained in the free-jet experiment performed by Gee et al. [21]. In this experiment, the Mach 1.8 ideally expanded free jet was generated using the same jet facility and nozzle as in Sec. II.A. The two-dimensional intensity probe consisted of four, parallel-axis 1/4 in. pressure microphones (G.R.A.S. 46BG) located at the vertices and center of an equilateral triangle, as shown in Fig. 8a. Four probes were attached to the two-axis positioning system during the experiment, as shown in Fig. 8b. Using these probes, the intensity vectors were obtained at the points shown in Fig. 9. The signals were acquired using the sound and vibration data acquisition module National Instruments PXI-4498 (sampling frequency = 204.8 kHz; signal length = 6.1 s).

The target frequency was determined as 13 kHz ($St = 0.54$), which was the same frequency as that focused on in the conditional sampling of the schlieren visualization movies in Sec. II.C. Figure 10 shows the acoustic intensity vectors and intensity level contours at 13 kHz. In the direction 30 deg from the jet axis, there is a high-intensity-level region, where the Mach waves dominate. In this analysis, the vectors dominated by the Mach waves were first selected from the vectors on the line located at $3D$ above the jet boundary, which was determined to be at an angle of 3.5 deg from the jet axis based on the schlieren images. The vector direction rapidly changes at $x/D \approx 7$, where there is also the contour line of 115 dB. Therefore, the vectors that have higher intensity levels than

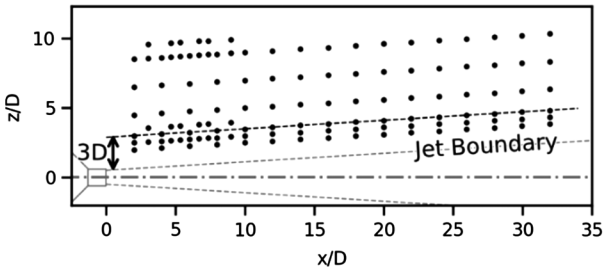

Fig. 9 Measurement points of acoustic intensity vectors (filled circles on the dashed line: measurement points for the ray-tracing analysis).

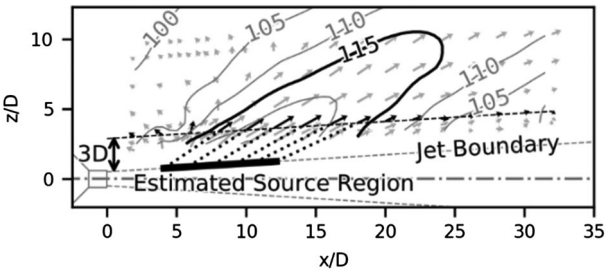

Fig. 10 Acoustic intensity vectors in the free-jet case at 13 kHz ($St = 0.54$).

115 dB on the black dashed line were selected as the target vectors dominated by the Mach waves.

By tracing back the selected vectors in a manner similar to that in Gee et al. [32], the source region can be estimated as the thick black line in Fig. 10. In the impinging jet case, only the vectors originating in the region upstream of the inclined flat plate are taken into consideration. Therefore, these vectors were selected and traced to the far field, assuming specular reflection at the inclined flat plate. Figures 11a and 11b show the tracing lines for the nozzle–plate distances of $5D$ and $15D$, respectively. Note that the vectors beneath the jet are drawn by assuming the axisymmetric acoustic field. The tracing lines indicate the propagation region of the Mach waves, which are radiated from the free-jet region, reflected by the inclined flat plate, and propagated to the far field in the impinging jet case. Figure 11b shows that all the selected vectors originate in the region upstream of the inclined flat plate for the nozzle–plate distance of $15D$. Thus, several tracing lines are drawn, which suggests that the propagation region of the Mach waves will be large. In contrast, Fig. 11a shows only a few tracing lines because most of the vectors originate in the region downstream of the inclined flat plate for the nozzle–plate distance of $5D$. This suggests that the effect of the Mach waves from the free-jet region on the acoustic field will be small in this case.

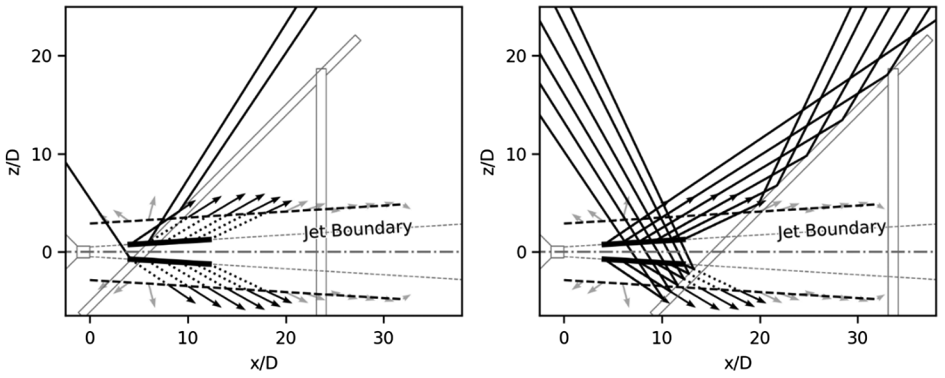

a) Nozzle–plate distance = 5*D* b) Nozzle–plate distance = 15*D*

Fig. 11 Tracing lines of the acoustic intensity vectors at 13 kHz ($St = 0.54$).

III. Results and Discussion

A. Comparison Between Images Extracted from the Schlieren Visualization Movies and Tracing Lines

This section discusses the differences in the acoustic field for the various nozzle–plate distances based on the results of the conditional sampling of the schlieren visualization movies and the tracing lines of the acoustic intensity vectors. As in Akamine et al. [19], two cases with different nozzle–plate distances (5*D* and 15*D*) are compared. The acoustic waves propagating at an angle of 75 deg from the inclined flat plate are the focus because there is a high OASPL region in this direction in both these cases, as explained in Sec. II.C.

Figure 12 shows the extracted results for the nozzle–plate distance of 15*D*. A density fluctuation appears first and propagates downstream along the free-jet region. Figure 12a shows the fluctuation at $\tau = -2.80$ ms. The fluctuation at point (i) in Fig. 12a moves to the location at point (i) in Fig. 12b after 0.25 ms. Subsequently, at $\tau = -2.30$ and -2.25 ms, Figs. 12c and 12d capture the fluctuations at points (ii) and (i′). The fluctuation at point (ii) propagates in a downstream direction. The fluctuation at point (i′) propagates at an angle of $\theta \approx 75$ deg, where the high OASPL is observed in Fig. 6b. The fluctuation at point (i′) propagates farther upward and appears in the region above the jet in Figs. 12e and 12f ($\tau = -2.10$ and -2.00 ms). At these times, the fluctuation at point (iii) also appears around the impingement region and propagates at an angle of $\theta \approx 75$ deg.

The fluctuations at points (i′) and (ii) in Figs. 12c–12f are the intermittent acoustic wave that is selected as the trigger because of the following two reasons: the fluctuations propagate in the direction of $\theta = 75$ deg, where the microphone for the trigger detection is located, and it is radiated from the impingement region at 2.2–2.3 ms before the trigger. This is consistent with the fact that it takes approximately 2.3 ms for an acoustic wave to propagate across the

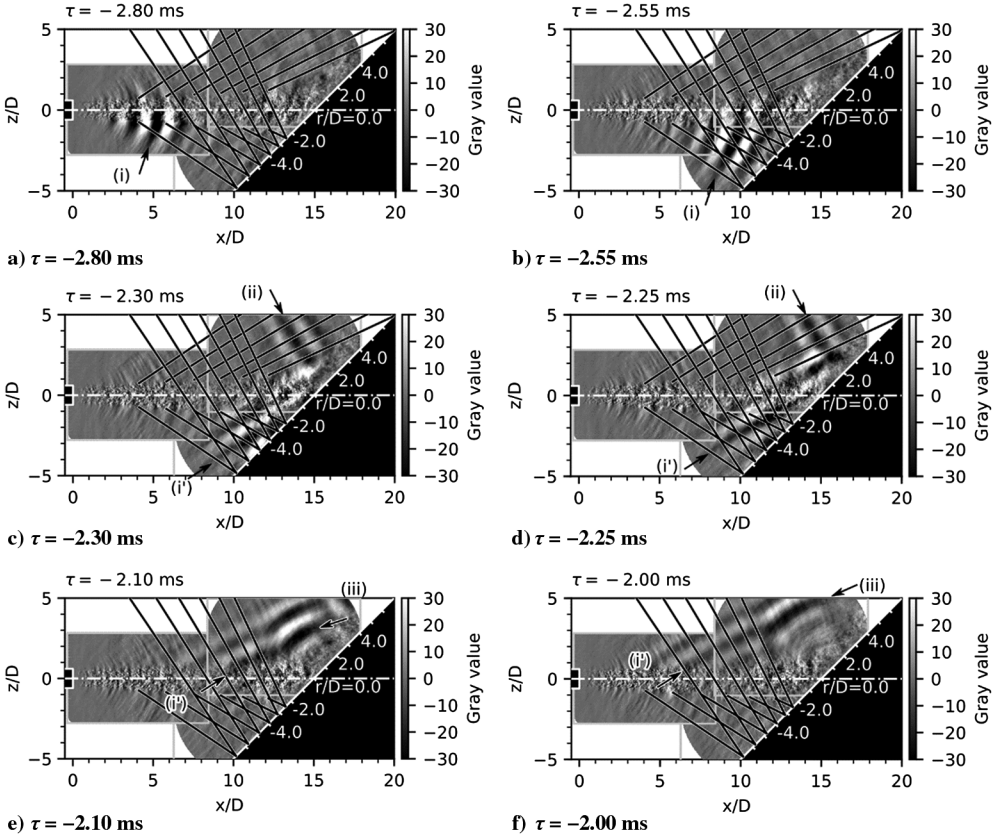

a) $\tau = -2.80$ ms b) $\tau = -2.55$ ms
c) $\tau = -2.30$ ms d) $\tau = -2.25$ ms
e) $\tau = -2.10$ ms f) $\tau = -2.00$ ms

Fig. 12 Extracted images (trigger microphone, $r/D = 40$ and $\theta = 75$ deg; trigger frequency, 13 kHz) and tracing lines of the acoustic intensity vectors (13 kHz) in the 15*D* case.

distance of $40D$ (0.8 m) between the impingement region and the microphone at the speed of sound (343 m/s).

The tracing lines are also drawn in Fig. 12. In Figs. 12a and 12b, the fluctuation at point (i) propagates along the tracing lines from the lower side of the free-jet region. This indicates that the fluctuation at point (i) will be the Mach waves from the lower side of the jet. The fluctuation at point (ii) in Figs. 12c and 12d propagates along the tracing lines from the upper side of the jet, which suggests that this will also be the Mach waves. The Mach waves at point (ii) are not discussed in this paper because they will not propagate in the target direction $\theta \approx 75$ deg after the reflection at the inclined flat plate, as shown in Fig. 11b. The fluctuation at point (i′) propagates along the tracing lines reflected below the jet. Therefore, this is the Mach waves at point (i) in Figs. 12a and 12b after the reflection at the inclined flat plate. In Figs. 12c–12f, the waves at point (i′) propagate from the lower side to the upper side of the free-jet region along the tracing lines. Because the tracing lines do not take into account the influences of the velocity profile or disturbances in the free-jet region, this suggests that some portion of the reflected Mach waves are refracting around the supersonic flow. Finally, the fluctuation at point (iii) cannot be regarded as the Mach waves or their reflected waves because the fluctuation at point (iii) originates in the impingement region above the jet and propagates in the region that is away from the tracing lines. This will be the acoustic waves generated in the impingement region. Thus, in the case of the nozzle–plate distance of $15D$, two types of acoustic waves propagate at an angle of $\theta \approx 75$ deg: the Mach waves from the lower side of the free-jet region, which are reflected by the inclined flat plate, and the acoustic waves generated in the impingement region.

Figure 13 shows the results extracted from the schlieren visualization movies for the nozzle–plate distance of $5D$. At 2.5 ms before the trigger ($\tau = -2.50$ ms), a density fluctuation appears in the free-jet region, as shown in Fig. 13a. This fluctuation propagates downstream along the free-jet region: the fluctuation at point (iv) in Fig. 13a moves to the location at point (iv) in Fig. 13b after 0.1 ms. This fluctuation reaches the impingement region, and then new fluctuations appear at $\tau = -2.10$ ms, as shown in Fig. 13c. These fluctuations originate in the impingement region: the fluctuations at points (v), (vi), and (vii) in Fig. 13c move to the locations at points (v), (vi), and (vii) in Fig. 13d, respectively, after 0.1 ms. The fluctuation at point (v) in Figs. 13c and 13d is the intermittently generated acoustic waves that are detected at the microphone because of the same reasons for the acoustic waves at points (i′) and (ii) for the nozzle–plate distance of $15D$.

Figures 13c and 13d show a comparison of the fluctuations (point (v)) and tracing lines. A tracing line is drawn from the lower side of the jet in the direction of $\theta = 75$ deg. This indicates that the Mach waves from the lower side of the free-jet region will propagate in the direction of $\theta = 75$ deg after its reflection at the inclined flat plate. The direction of the tracing line is similar to the propagation direction of the acoustic waves (point (v)) of the extracted results. However, the acoustic waves (point (v)) propagate in a wider region than that indicated by the tracing line. In addition, the acoustic waves (point (v)) originate at the upper side of the impingement region. Therefore, the acoustic waves (point (v)) cannot be regarded as the Mach waves from the lower side of the free-jet region; they are the acoustic waves generated in the impingement region. This consideration is consistent with the result of the ray tracing shown in Fig. 11a, in which the jet impinges on the inclined flat plate before most of the Mach waves are generated from the free jet region. As for the fluctuation (point (iv)) in Figs. 13a and 13b, similar flow structures also appear in the free-jet region in Fig. 12a, in the $15D$ case, and they are extracted because they relate to the generation of the Mach waves in the free-jet region, and the Mach waves are detected at the microphone after reflection at the plate. However, the impingement occurs before the Mach waves have fully formed in the $5D$ case. Therefore, the fluctuation (point (iv)) is extracted because it correlates to the microphone signal via the acoustic waves generated in the impingement region, instead of the reflected Mach waves, in the $5D$ case.

The preceding results show an important difference in the Mach waves reflected by the inclined flat plate between the two cases of nozzle–plate distances of $5D$ and $15D$. The difference in the nozzle–plate distance changes the location of the inclined flat plate relative to the source region of the Mach waves in the free-jet region. For the nozzle–plate distance of $5D$, impingement occurs before the Mach waves have fully formed. Consequently, the acoustic waves observed in the target direction, $\theta \approx 75$ deg, are strongly correlated only with the acoustic waves generated in the impingement region in the $5D$ case. For the $15D$ case, Mach wave radiation also reflects from the plate such that there is high correlation between both the Mach waves and the acoustic waves generated in the impingement region and the observed acoustic waves at $\theta = 75$ deg.

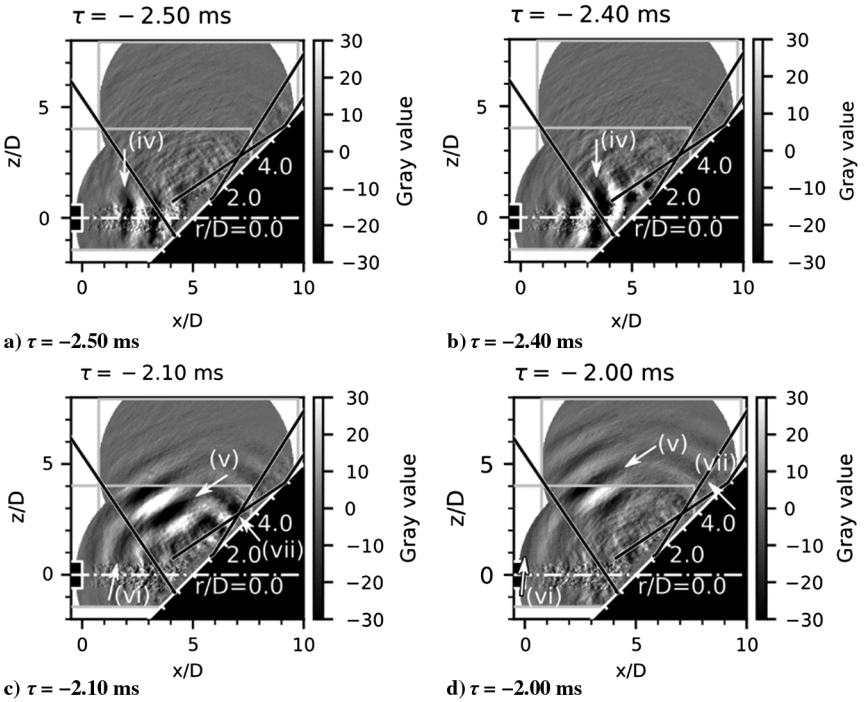

Fig. 13 Extracted images (trigger microphone, $r/D = 40$ and $\theta = 75$ deg; trigger frequency, 13 kHz) and tracing lines of the acoustic intensity vectors (13 kHz) in the $5D$ case.

B. Comparison Between Overall Sound Pressure Level Distributions and Tracing Lines

This section discusses the OASPL distributions based on the considerations of the previous section. Figure 14 shows the OASPL distributions in the cases of four nozzle–plate distances, in which the cases of $5D$ and $15D$ have been previously presented in [19]. Although a high-OASPL region appears at $\theta \approx 75$ deg in all the cases, the OASPL at $\theta \approx 75$ deg differs, owing to the nozzle–plate distances. In particular, the OASPLs at $r/D = 40$ and $\theta = 75$ deg in the $10D$, $15D$, and $20D$ cases (filled circle in Fig. 14) are more than

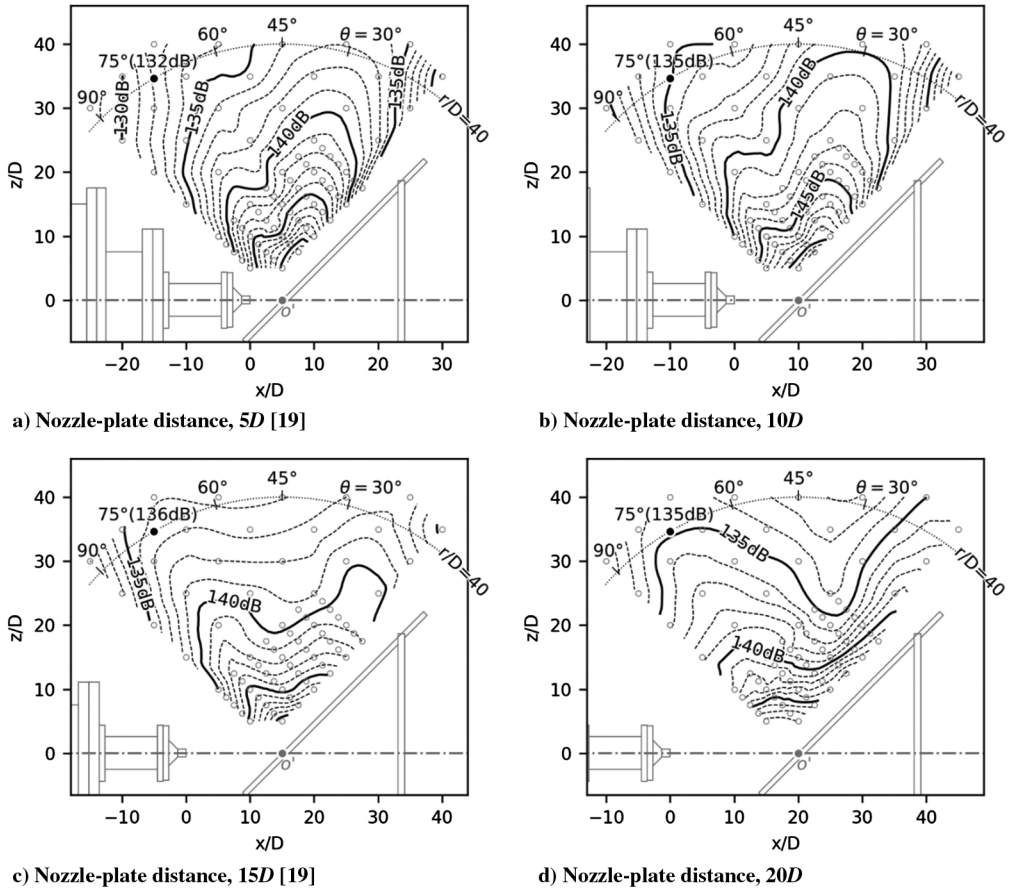

Fig. 14 OASPL distribution (filled circle, $r/D = 40$ and $\theta = 75$ deg, where the microphone located to detect the triggers).

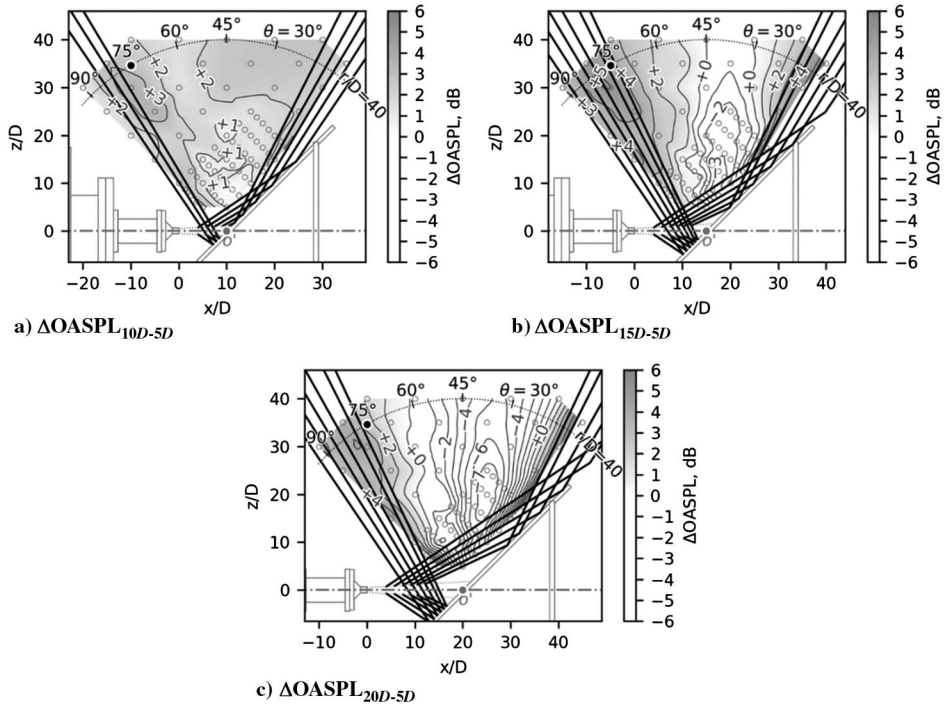

Fig. 15 Comparison between ΔOASPL and tracing lines at 13 kHz, $St = 0.54$ (filled circle, $r/D = 40$ and $\theta = 75$ deg, where the microphone is located to detect the triggers).

3 dB higher than that in the 5D case. This increase in OASPL is the main focus in this study.

According to the previous section, the nozzle–plate distance affects the fraction of the Mach waves that are generated in the free-jet region and reflected by the inclined plate. In the 5D case, the acoustic waves from the impingement region propagate in the direction of $\theta \approx 75$ deg, as shown in Fig. 12. This suggests that the high-OASPL region in the direction of $\theta \approx 75$ deg in Fig. 14a occurs mainly due to the acoustic waves generated in the impingement region. In contrast, in the 15D case, both the reflected Mach waves and acoustic waves generated in the impingement region will propagate in the direction of $\theta \approx 75$ deg and therefore contribute to the high-OASPL region in Fig. 14c. This may be related to the increase in the OASPL in the direction of $\theta \approx 75$ deg.

To make this relation clearer, Fig. 15 shows a comparison of the tracing lines and distributions of ΔOASPL, which is defined as follows:

$$\Delta\mathrm{OASPL}_{kD-5D}(x,z) = \mathrm{OASPL}_{kD}(x,z) - \mathrm{OASPL}_{5D}(x-5D+kD,z) \quad (k = 10, 15, \text{and } 20) \tag{4}$$

The OASPL in the 5D case, when the reflected Mach waves are not dominant in the direction of $\theta \approx 75$ deg, is subtracted from that at the same location, relative to the inclined flat plate, in the other cases. In these ΔOASPL maps, there are various features, which may be caused by the reflected Mach waves, the acoustic waves generated in the impingement region, and the Mach waves from the wall-jet region. The main focus in this paper is the high-ΔOASPL region in the range of $\theta = 75$–90 deg for all the cases. Moreover, it can be found that this region almost corresponds to the tracing lines. This indicates that the OASPL in the 10D, 15D, and 20D cases is higher than that in the 5D case in the region where the reflected Mach waves propagate. Therefore, the OASPL increase in the direction of $\theta \approx 75$ deg is mainly caused by this difference in the reflected Mach waves.

IV. Conclusions

This study experimentally discussed the effect of the nozzle–plate distance on the broadband acoustic field of a supersonic jet impinging on an inclined flat plate. The motivation of this study was to clarify the reason why the OASPL becomes higher in the upstream region (in particular, in the direction of 75 deg from the inclined flat plate) in longer nozzle–plate distance cases than in a shorter case. The previous studies suggested that there were two possible factors that cause the differences in the acoustic field: the acoustic waves generated in the impingement region and the Mach waves, which were radiated from the free-jet region and reflected by the plate. To distinguish the effects of the influencing factors, the tracing lines showing the propagation region of the reflected Mach waves were estimated by introducing the ray-tracing technique of the acoustic intensity vectors of the Mach waves obtained in the free-jet experiment. The tracing lines were compared with the images extracted from the schlieren visualization movies using acoustic-triggered conditional sampling. The results revealed that the nozzle–plate distance affects the fraction of the Mach waves that are generated in the free-jet region and reflected by the inclined plate. In the case of the shorter nozzle–plate distance of 5D, only the acoustic waves generated in the impingement region propagate in the direction of 75 deg from the inclined flat plate, whereas both these waves and the reflected Mach waves propagate in the same direction in the case of the longer nozzle–plate distance (15D case). Moreover, the propagation region of the reflected Mach waves almost agreed with the region where the OASPL for the 10D, 15D, and 20D cases becomes higher than that in the 5D case. This indicated that the reflected Mach waves contribute to this OASPL increase, which is an important difference in the acoustic field. Consequently, the obtained results revealed that the location of the inclined flat plate relative to the source region of the Mach waves is an important factor for understanding the effect of the nozzle–plate distance on the acoustic field.

This work has quantified the difference in acoustic phenomena for nozzle–plate distances of 5D and 15D, but many questions remain. This work has not attempted to separate the different components and uncover the nature of the impingement noise. It is possible that multiple acoustic triggers could be used in future investigations to answer these questions. In addition, subsequent studies are needed to evaluate the acoustics for different nozzle–plate distances to better understand the continually varying acoustic environment during a rocket launch.

Acknowledgments

A portion of this study was supported by an Invitation Fellowship from the Japan Society for the Promotion of Science (JSPS) and the Grant-in-Aid for JSPS Research Fellow (grant 16J08627). The authors would like to thank Chihiro Konno of the University of Tokyo and George Kuwabara of Photron Limited. The authors would also like to express their appreciation to Darren K. Torrie and Eric B. Whiting of Brigham Young University for their assistance.

References

[1] Henderson, B., "The Connection Between Sound Production and Jet Structure of the Supersonic Impinging Jet," *Journal of the Acoustical Society of America*, Vol. 111, No. 2, 2002, pp. 735–747. doi:10.1121/1.1436069

[2] Henderson, B., Bridges, J., and Wernet, M., "An Experimental Study of the Oscillatory Flow Structure of Tone-Producing Supersonic Impinging Jets," *Journal of Fluid Mechanics*, Vol. 542, Nov. 2005, pp. 115–137. doi:10.1017/S0022112005006385

[3] Risborg, A., and Soria, J., "High-Speed Optical Measurements of an Underexpanded Supersonic Jet Impinging on an Inclined Plate," *Proceedings of the 28th International Congress on High-Speed Imaging and Photonics*, International Soc. for Optics and Photonics Paper 71261F, Bellingham, WA, 2009.

[4] Dauptain, A., Gicquel, L. Y. M., and Moreau, S., "Large Eddy Simulation of Supersonic Impinging Jets," *AIAA Journal*, Vol. 50, No. 7, 2012, pp. 1560–1574. doi:10.2514/1.J051470

[5] Weightman, J. L., Amili, O., Honnery, D., Soria, J., and Edgington-Mitchell, D., "An Explanation for the Phase Lag in Supersonic Jet Impingement," *Journal of Fluid Mechanics*, Vol. 815, March 2017, p. R1. doi:10.1017/jfm.2017.37

[6] Gojon, R., and Bogey, C., "Flow Structure Oscillations and Tone Production in Underexpanded Impinging Round Jets," *AIAA Journal*, Vol. 55, No. 6, 2017, pp. 1792–1805. doi:10.2514/1.J055618

[7] Uzun, A., Kumar, R., Hussaini, M. Y., and Alvi, F. S., "Simulation of Tonal Noise Generation by Supersonic Impinging Jets," *AIAA Journal*, Vol. 51, No. 7, 2013, pp. 1593–1611. doi:10.2514/1.J051839

[8] Kumar, R., Wiley, A., Venkatakrishnan, L., and Alvi, F., "Role of Coherent Structures in Supersonic Impinging Jets," *Physics of Fluids*, Vol. 25, No. 7, 2013, Paper 076101. doi:10.1063/1.4811401

[9] Davis, T., Edstrand, A., Alvi, F., Cattafesta, L., Yorita, D., and Asai, K., "Investigation of Impinging Jet Resonant Modes Using Unsteady Pressure-Sensitive Paint Measurements," *Experiments in Fluids*, Vol. 56, No. 5, 2015, p. 101. doi:10.1007/s00348-015-1976-9

[10] Nonomura, T., Goto, Y., and Fujii, K., "Aeroacoustic Waves Generated from a Supersonic Jet Impinging on an Inclined Flat Plate," *International Journal of Aeroacoustics*, Vol. 10, No. 4, 2011, pp. 401–425. doi:10.1260/1475-472X.10.4.401

[11] Tam, C. K. W., "Mach Wave Radiation from High-Speed Jets," *AIAA Journal*, Vol. 47, No. 10, 2009, pp. 2440–2448. doi:10.2514/1.42644

[12] Tsutsumi, S., Takaki, R., Nakanishi, Y., Okamoto, K., and Teramoto, S., "Numerical Study on Acoustic Radiation from a Supersonic Jet Impinging to an Inclined Plate," *17th AIAA/CEAS Aeroacoustics Conference*, AIAA Paper 2011-2922, June 2011.

[13] Tsutsumi, S., Takaki, R., Nakanishi, Y., Okamoto, K., and Teramoto, S., "Acoustic Generation Mechanism of a Supersonic Jet Impinging on Deflectors," *52nd AIAA Aerospace Sciences Meeting*, AIAA Paper 2014-0882, Jan. 2014.

[14] Brehm, C., Housman, J. A., and Kiris, C. C., "Noise Generation Mechanisms for a Supersonic Jet Impinging on an Inclined Plate," *Journal of Fluid Mechanics*, Vol. 797, June 2016, pp. 802–850. doi:10.1017/jfm.2016.244

[15] Nonomura, T., Honda, H., Nagata, Y., Yamamoto, M., Morizawa, S., Obayashi, S., and Fujii, K., "Plate-Angle Effects on Acoustic Waves from Supersonic Jets Impinging on Inclined Plates," *AIAA Journal*, Vol. 54, No. 3, 2016, pp. 816–827. doi:10.2514/1.J054152

[16] Worden, T. J., Gustavsson, J. P. R., Shih, C., and Alvi, F. S., "Acoustic Measurements of High-Temperature Supersonic Impinging Jets in Multiple Configurations," *19th AIAA/CEAS Aeroacoustics Conference*, AIAA Paper 2013-2187, May 2013.

[17] Worden, T. J., Shih, C., and Alvi, F. S., "Supersonic Jet Impingement on a Model-Scale Jet Blast Deflector," *AIAA Journal*, Vol. 55, No. 8, 2017, pp. 2522–2536. doi:10.2514/1.J055664

[18] Akamine, M., Nakanishi, Y., Okamoto, K., Teramoto, S., Okunuki, T., and Tsutsumi, S., "Acoustic Phenomena from Correctly Expanded Supersonic Jet Impinging on Inclined Plate," *AIAA Journal*, Vol. 53, No. 7, 2015, pp. 2061–2067. doi:10.2514/1.J053953

[19] Akamine, M., Okamoto, K., Teramoto, S., Okunuki, T., and Tsutsumi, S., "Conditional Sampling Analysis of Acoustic Phenomena from Supersonic Jet Impinging on Inclined Flat Plate," *Transactions of the Japan Society for Aeronautical and Space Sciences*, Vol. 59, No. 5, 2016, pp. 287–294. doi:10.2322/tjsass.59.287

[20] Tsutsumi, S., Takaki, R., Shima, E., Fujii, K., and Arita, M., "Generation and Propagation of Pressure Waves from H-IIA Launch Vehicle at Lift-Off," *48th AIAA Aerospace Sciences Meeting and Exhibit*, AIAA Paper 2008-0390, Jan. 2008.

[21] Gee, K. L., Neilsen, T. B., Sommerfeldt, S. D., Akamine, M., and Okamoto, K., "Experimental Validation of Acoustic Intensity Bandwidth Extension by Phase Unwrapping," *Journal of the Acoustical Society of America*, Vol. 141, No. 4, 2017, pp. EL357–EL362. doi:10.1121/1.4979604

[22] Moore, C. J., "The Role of Shear-Layer Instability Waves in Jet Exhaust Noise," *Journal of Fluid Mechanics*, Vol. 80, No. 2, 1977, pp. 321–367. doi:10.1017/S0022112077001700

[23] Camussi, R., and Guj, G., "Experimental Analysis of Intermittent Coherent Structures in the Near Field of a High *Re* Turbulent Jet Flow," *Physics of Fluids*, Vol. 11, No. 2, 1999, pp. 423–431. doi:10.1063/1.869859

[24] Guj, G., Carley, M., and Camussi, R., "Acoustic Identification of Coherent Structures in a Turbulent Jet," *Journal of Sound and Vibration*, Vol. 259, No. 5, 2003, pp. 1037–1065. doi:10.1006/jsvi.2002.5130

[25] Cavalieri, A. V. G., Jordan, P., Gervais, Y., Wei, M., and Freund, J. B., "Intermittent Sound Generation and Its Control in a Free-Shear Flow," *Physics of Fluids*, Vol. 22, No. 11, 2010, Paper 115113. doi:10.1063/1.3517297

[26] Kœnig, M., Cavalieri, A. V. G., Jordan, P., Delville, J., Gervais, Y., and Papamoschou, D., "Farfield Filtering and Source Imaging of Subsonic Jet Noise," *Journal of Sound and Vibration*, Vol. 332, No. 18, 2013, pp. 4067–4088. doi:10.1016/j.jsv.2013.02.040

[27] Hileman, J. I., Thurow, B. S., Caraballo, E. J., and Samimy, M., "Large-Scale Structure Evolution and Sound Emission in High-Speed Jets: Real-Time Visualization with Simultaneous Acoustic Measurements," *Journal of Fluid Mechanics*, Vol. 544, Dec. 2005, pp. 277–307. doi:10.1017/S002211200500666X

[28] Kastner, J., Samimy, M., Hileman, J., and Freund, J. B., "Comparison of Noise Mechanisms in High and Low Reynolds Number High-Speed Jets," *AIAA Journal*, Vol. 44, No. 10, 2006, pp. 2251–2258. doi:10.2514/1.18384

[29] Torrence, C., and Compo, G. P., "A Practical Guide to Wavelet Analysis," *Bulletin of the American Meteorological Society*, Vol. 79, No. 1, 1998, pp. 61–78. doi:10.1175/1520-0477(1998)079%3C0061:APGTWAtpmkset%20

[30] Thomas, D. C., Christensen, B. Y., and Gee, K. L., "Phase and Amplitude Gradient Method for the Estimation of Acoustic Vector Quantities," *Journal of the Acoustical Society of America*, Vol. 137, No. 6, 2015, pp. 3366–3376. doi:10.1121/1.4914996

[31] Mann, J. A., III, Tichy, J., and Romano, A. J., "Instantaneous and Time-Averaged Energy Transfer in Acoustic Fields," *Journal of Acoustical Society of America*, Vol. 82, No. 1, 1987, pp. 17–30. doi:10.1121/1.395562

[32] Gee, K. L., Whiting, E. B., Neilsen, T. B., James, M. M., and Salton, A. R., "Development of a Near-Field Intensity Measurement Capability for Static Rocket Firings," *Transactions of the Japan Society for Aeronautical and Space Sciences, Aerospace Technology Japan*, Vol. 14, No. 30, 2016, pp. Po_2_9–Po_2_15. doi:10.2322/tastj.14.Po_2_9

C. Bailly
Associate Editor